nature COMMUNICATIONS

ARTICLE

https://doi.org/10.1038/s41467-019-10084-5 OPEN

Plasmonic photosynthesis of C_1–C_3 hydrocarbons from carbon dioxide assisted by an ionic liquid

Sungju Yu [1] & Prashant K. Jain [1,2,3,4]

Photochemical conversion of CO_2 into fuels has promise as a strategy for storage of intermittent solar energy in the form of chemical bonds. However, higher-energy-value hydrocarbons are rarely produced by this strategy, because of kinetic challenges. Here we demonstrate a strategy for green-light-driven synthesis of C_1–C_3 hydrocarbons from CO_2 and H_2O. In this approach, plasmonic excitation of Au nanoparticles produces a charge-rich environment at the nanoparticle/solution interface conducive for CO_2 activation, while an ionic liquid stabilizes charged intermediates formed at this interface, facilitating multistep reduction and C–C coupling. Methane, ethylene, acetylene, propane, and propene are photosynthesized with a C_{2+} selectivity of ~50% under the most optimal conditions. Hydrocarbon turnover exhibits a volcano relationship as a function of the ionic liquid concentration, the kinetic analysis of which coupled with density functional theory simulations provides mechanistic insights into the synergy between plasmonic excitation and the ionic liquid.

[1] Department of Chemistry, University of Illinois at Urbana-Champaign, Urbana, Illinois 61801, USA. [2] Department of Physics, University of Illinois at Urbana-Champaign, Urbana, Illinois 61801, USA. [3] Materials Research Laboratory, University of Illinois at Urbana-Champaign, Urbana, Illinois 61801, USA. [4] Beckman Institute of Advanced Science and Technology, University of Illinois at Urbana-Champaign, Urbana, Illinois 61801, USA. Correspondence and requests for materials should be addressed to P.K.J. (email: jain@illinois.edu)

Carbon dioxide (CO_2) fixation is recognized to be a much-needed component of a carbon-neutral energy strategy[1–4]. Although CO_2 is relatively unreactive, various catalytic processes triggered by heat (thermochemical)[5–8], electricity (electrochemical)[9–17], and light (photochemical)[18–28] are being explored for activating CO_2 and recycling it back to valuable petrochemicals. Sunlight-driven conversion of CO_2 to fuels is particularly attractive as a means to store intermittent solar energy in the form of C–C and C–H bonds. Semiconductor and metal-catalyzed photoelectrolytic reduction of CO_2 has shown promise; however, these processes have often required ultraviolet (UV) light and/or considerable electrical energy input, or they do not favor energy-rich hydrocarbon products. Longer-chain hydrocarbons possess higher energy densities. Moreover, hydrocarbons in the liquid state are easier to transport[29,30]. However, the formation of longer-chain hydrocarbons from CO_2 requires multiple electron (e^-) and proton (H^+) transfer steps, as well as C–C bond formation[9,31,32], which pose major kinetic bottlenecks.

Here we demonstrate a visible-light-driven route for the conversion of CO_2 and H_2O into C_1–C_3 hydrocarbons. The scheme does not involve the application of an electrochemical potential, UV light, high temperatures, hydrogen gas, or a sacrificial agent. It uses green light as the sole energy input and driving agent. The strategy employs plasmonic Au nanoparticles (NPs) of a pseudospherical shape and an average diameter of ~12 nm, as characterized previously[28]. Au NPs are known from electrochemical studies[33] to activate CO_2. The choice of Au NPs was further driven by the relative chemical stability of Au against bulk oxidation and photocorrosion; the other two common plasmonic metals, Ag and Cu, while electrocatalytically active for CO_2 reduction, are prone to oxidation in air, water, and/or light excitation. The Au NPs possess a strong localized surface plasmon resonance (LSPR) band centered around 520 nm (Fig. 1a), which enables strong, resonant absorption of green light. The LSPR excitation of the NPs yields energetic electron–hole (e^-–h^+) carriers via Landau damping. These e^-–h^+ carriers were shown in recent studies to drive redox conversions[28,34–36], especially the conversion of CO_2 to methane and ethane under blue–green light[28]. However, in this past demonstration, isopropanol was used as a sacrificial h^+ scavenger to facilitate e^-–h^+ pair separation; otherwise, unproductive e^-–h^+ recombination dominated. Thus, isopropanol served as the H^+ source in this CO_2 reduction scheme, which posed a major limitation for net energy storage.

The present strategy overcomes this drawback and uses water as the H^+ source and does not require a sacrificial h^+ scavenger, thus constituting a truly fuel-forming reaction. The enhanced reactivity was enabled by the use of an ionic liquid (IL) medium, specifically comprised 1-ethyl-3-methylimidazolium tetrafluoroborate (EMIM-BF_4). Our choice was motivated by examples from electrocatalytic CO_2 reduction reaction (CO_2RR) where the EMIM-BF_4 electrolyte, owing to its highly ionic character, stabilizes the high-energy $CO_2^{\bullet-}$ radical anion intermediate formed in the reaction and decreases the overpotential needed for CO_2RR[37–42]. In addition, EMIM-BF_4 has a wide electrochemical window and high thermal stability[43,44]. In our photocatalytic scheme, the EMIM-BF_4, as we find from kinetic analysis and density functional theory (DFT) simulations, promotes e^- transfer at the interface of the photoexcited Au NP and adsorbed CO_2 (Fig. 1b), obviating the need for a h^+ scavenger or applied potential for e^-–h^+ separation.

Results

IL-mediated plasmonic CO_2 reduction. The photocatalyst had the form of a substrate-supported film of Au NPs immersed in an aqueous solution of EMIM-BF_4 saturated with CO_2 and contained inside a glass reactor (Supplementary Methods). The light excitation source comprised a continuous-wave (CW) laser of a wavelength of 532 nm light and an intensity of 1 W cm^{-2}. Under CW excitation, the steady-state temperature of the reaction medium got moderately elevated to ~48 °C. Hydrocarbon products collected in the reactor headspace were measured (Supplementary Figs. 1−11) using a gas chromatograph (GC) equipped with a flame ionization detector. The EMIM-BF_4 concentration was varied from 0 to 100 mol%, to find optimal conditions for CO_2RR. In 1–10 mol% EMIM-BF_4, the products of plasmon-excitation-driven CO_2RR were found to be C_1 (CH_4), C_2 (C_2H_4 and C_2H_2), and highly reduced C_3 (C_3H_6 and C_3H_8) hydrocarbons (Fig. 1c, d and Supplementary Note 1). This product profile is quite striking when one considers that the major product in electrochemical CO_2RR is carbon monoxide (CO) formed by $2e^-$–$2H^+$ reduction of CO_2 (refs. [13–17]). On the other hand, propane (C_3H_8), formed in our scheme, requires an overall $20e^-$–$20\ H^+$ reduction and coupling of three CO_2 molecules. Such generation of C_3 hydrocarbons by artificial photosynthesis is challenging and therefore rare.

The CO_2RR activity depends on the IL concentration (Fig. 1c). In pure water the activity was nil, whereas in 1 mol% EMIM-BF_4 solution the generation of C_1, C_2, and C_3 hydrocarbons was observed. The CO_2RR activity, as quantified by turnover frequencies (TOFs) of the hydrocarbon products, increased dramatically with an increase in the EMIM-BF_4 concentration. The highest activity was found at 5 mol% EMIM-BF_4. Increasing the EMIM-BF_4 concentration further resulted in a sharp drop in the CO_2RR activity. In 100 mol% EMIM-BF_4 solution, the activity was nil, similar to that in pure water. Thus, the CO_2RR activity exhibits a volcano relationship as a function of the EMIM-BF_4 concentration (Fig. 1c). At all EMIM-BF_4 concentrations, where C_1, C_2, and C_3 hydrocarbons were produced, the product selectivity was found to follow the order: $C_1 > C_2 > C_3$. The selectivity for C_{2+} production is ~50% in 1−10 mol% EMIM-BF_4 solution (Fig. 1d).

Non-hydrocarbon products were also characterized by a GC equipped with a thermal conductivity detector (TCD) (Supplementary Figs. 12–15). Considerable hydrogen (H_2) production was measured (Supplementary Fig. 12), the TOF of which was 138.2 $NP^{-1}\ h^{-1}$ in 5 mol% EMIM-BF_4 solution, the IL concentration where CO_2RR activity is the highest. The H_2 likely originates from the competing reduction of H^+ in the reaction medium (Supplementary Eq. (6)). In the GC-TCD measurements, there were no detection of CO (Supplementary Fig. 15), otherwise known to be a major product in electrocatalytic CO_2RR on Au (refs. [13–17]). Of the possible oxidation products, there was no measurable production of O_2 (see Supplementary Information). H_2O_2 was detected (Supplementary Figs. 16–18) by the fluorogenic test employing a amplex red and horseradish peroxidase reagent[45]. Thus, the oxidation of H_2O to H_2O_2 and H^+ ($2H_2O \rightarrow H_2O_2 + 2H^+ + 2e^-$) is the likely oxidation half-reaction that consumes the photogenerated h^+.

Control studies were performed, one without Au NPs, another without light, and a third without CO_2. The conditions were otherwise maintained the same as those in the photoreaction tests and a 5 mol% EMIM-BF_4 solution, found to be most optimal in the photoreaction tests, was employed. The control studies showed that the absence of any one of the components Au NPs, green light illumination, or CO_2 resulted in nil hydrocarbon production, despite the use of 5 mol% EMIM-BF_4 solution (Supplementary Fig. 19a–c). Thus, it is confirmed that the hydrocarbon production originates from green-light-driven CO_2 reduction on Au NPs. The control study without light excitation was performed at an elevated temperature of 50 °C so as to mimic

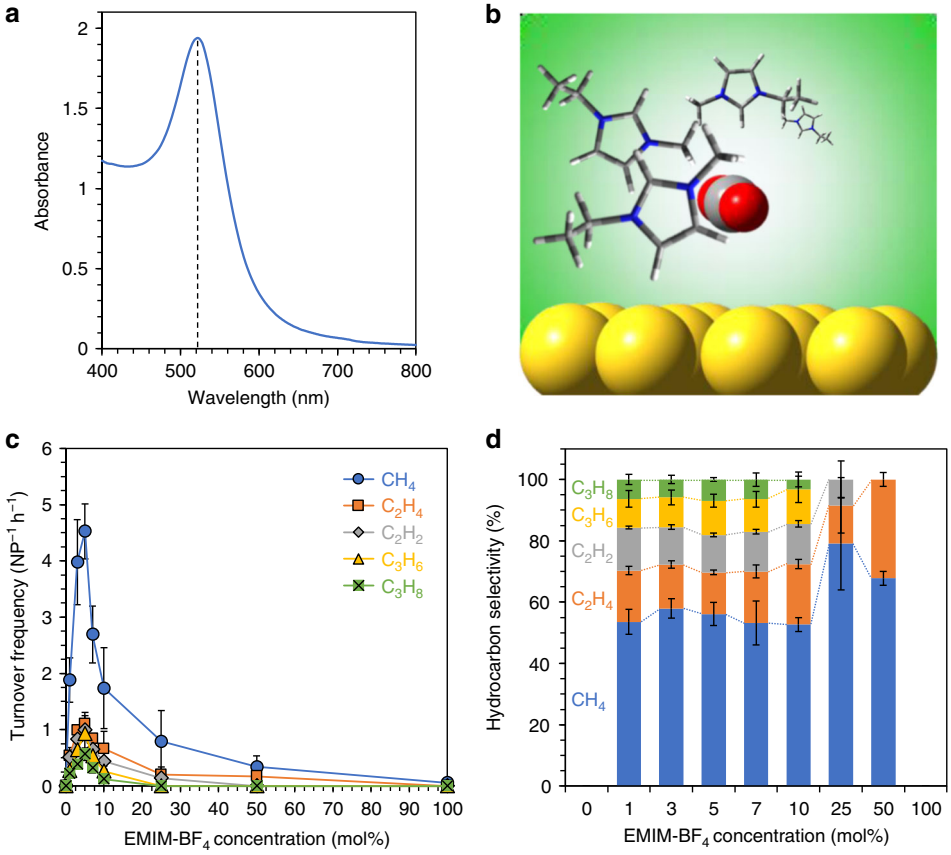

Fig. 1 Ionic-liquid-promoted CO_2 reduction to C_1–C_3 hydrocarbons using a plasmonic Au nanoparticle (NP) photocatalyst. **a** UV−vis extinction spectrum of a colloid of the Au NPs used for preparation of the photocatalyst film. The spectrum exhibits a localized surface plasmon resonance (LSPR) band centered around 520 nm, as indicated by the dotted line. **b** Scheme for CO_2 conversion on plasmon-excited Au NPs promoted by an ionic liquid, EMIM-BF_4. A continuous-wave (CW) laser of a wavelength of 532 nm and intensity of 1 W cm^{-2} was used as the light source for photoexcitation of Au NPs. EMIM-BF_4 stabilizes CO_2 and resulting adsorbates/intermediates on the photoexcited Au surface. **c** Turnover frequencies of hydrocarbon products formed in the CO_2RR plotted as a function of the EMIM-BF_4 concentration (mol%). The CO_2 conversion activity peaks at 5 mol% of EMIM-BF_4. **d** Hydrocarbon product selectivity as a function of EMIM-BF_4 concentration (mol%). Each data point in **c** and **d** is the average of results from three identical trials and the error bar represents the SD of these measurements

the steady-state bulk solution temperature of the reaction mixture in the photoreaction tests. The lack of CO_2RR activity in this dark control study demonstrates that the CO_2RR activity in the photoreaction tests does not originate from simply a photothermal effect of the light excitation. Rather a photoredox process facilitated by the Au NPs and the IL is responsible for the conversion of CO_2 to hydrocarbons.

The plasmonic catalyst also exhibited stability and recyclability under the photoreaction conditions and IL media subjected on the catalyst. We tested the same substrate-supported Au NP film immersed in 5 mol% EMIM-BF_4 over multiple cycles, each consisting of a 10 h photoreaction. The CO_2RR activity and product selectivity, as determined from the TOFs of the hydrocarbon products, was maintained over the course of this multi-cycle test (Supplementary Fig. 20). As the NP film or EMIM-BF_4 solution were not replenished between cycles, the maintenance of CO_2RR activity over multiple cycles suggests that Au and EMIM-BF_4 were not consumed, at any discernible levels, in the photoredox reaction.

The origin of products. Given the hydrocarbon profile of the product mixture, it was necessary to go beyond the control studies described above and confirm more directly that CO_2, rather than carbon contamination or photolysis of the EMIM-BF_4, was the source of the hydrocarbon products. For this confirmation, ^{13}C isotope labeling was employed (Fig. 2 and Supplementary Figs. 21 and 22). In this labeling study, $^{13}CO_2$ was employed as the reactant instead of $^{12}CO_2$, whereas all other conditions were kept the same as those in other photoreaction tests. GC-mass spectrometry (GC-MS) was used for identification of the hydrocarbon products generated in the photoreaction (Fig. 2a). The GC-MS analysis confirmed the presence of $^{13}CH_4$ (Fig. 2b) and $^{13}C_2H_2$ (Fig. 2c), manifested by their characteristic mass fragmentation patterns, shifted to higher m/z compared with reference fragmentation patterns of $^{12}CH_4$ and $^{12}C_2H_2$, respectively. Thus, isotope labeling confirms CO_2 to be the origin of hydrocarbon products.

The role of the IL. We attempted to gain a mechanistic understanding of this catalytic scheme focusing on the question of how the IL promotes CO_2RR activity. It was observed that the presence of EMIM-BF_4 in the aqueous medium results in a considerably acidic pH (Supplementary Fig. 23): the 5 mol% EMIM-BF_4 solution has a pH of 2.95. To determine whether this acidity is responsible for the enhanced CO_2RR activity in a EMIM-BF_4 solution, we performed a photoreaction in deionized water containing no EMIM-BF_4 but with a pH of 2.93 achieved using acid (Supplementary Fig. 19d). All other conditions were kept the same as in the photoreactions in EMIM-BF_4 solutions. In this EMIM-BF_4-free photoreaction, no products were observed, which demonstrated that the high acidity or H^+ concentration, [H^+], of

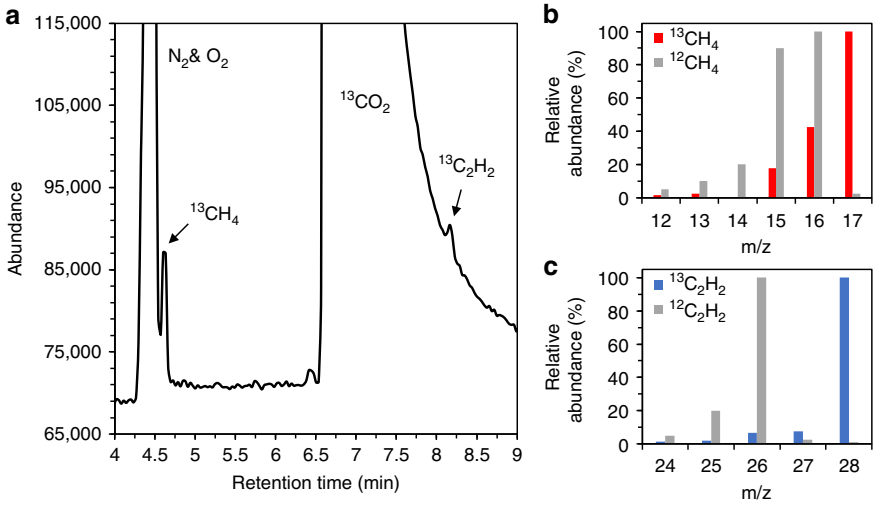

Fig. 2 $^{13}CO_2$ isotopolog confirmation of CO_2RR. **a** Total ion chromatogram (TIC) of the gaseous products from a 240 h long Au NP-photocatalyzed $^{13}CO_2$RR in 5 mol% EMIM-BF_4 solution under CW irradiation of 532 nm light (1 W cm^{-2}). Peaks in the TIC appearing at retention times of 4.6 min and 8.2 min correspond to $^{13}CH_4$ and $^{13}C_2H_2$. The basis for this assignment is provided in Supplementary Fig. 22. **b** Mass fragmentation pattern (red bars) acquired at a retention time of 4.6 min of the TIC shown in **a**. For comparison, a reference fragmentation pattern (gray bars) of $^{12}CH_4$ from the National Institute of Standards and Technology (NIST) Chemistry WebBook is shown. Fragments at m/z = 14 and 18 in the experimental pattern were suppressed to remove the mass peaks contributed by N_2 and moisture, respectively. **c** Mass fragmentation pattern (blue bars) acquired at a retention time of 8.2 min of the TIC shown in **a**. For comparison, a reference fragmentation pattern (gray bars) of $^{12}C_2H_2$ from the NIST Chemistry WebBook is shown. The fragment at m/z = 28 in the experimental pattern has relatively high abundance as compared with that of the reference fragmentation pattern due to the contribution of N_2 from the atmosphere. Relative abundances in **b** and **c** were obtained from the measured abundances shown in Supplementary Fig. 21a, b, respectively. It is noteworthy that $^{13}C_2H_4$ was not resolved by GC-MS due to the likely overlap of the $^{13}C_2H_4$ peak with the broad, intense $^{13}CO_2$ peak in the TIC (Supplementary Fig. 22b)

the EMIM-BF_4-containing medium is not the sole cause of the enhanced CO_2RR activity. EMIM-BF_4 plays other role(s). It is possible, in principle, for EMIM-BF_4, instead of H_2O, to serve as the h^+ acceptor; however, if this were the case, then the CO_2RR activity would have been enhanced at higher EMIM-BF_4 concentrations, in line with a study of a different plasmon excitation-catalyzed redox reaction[36]. Instead, we observed peak activity at a EMIM-BF_4 concentration of 5 mol%, above which the activity drops steeply reaching nil in pure EMIM-BF_4 wherein H_2O is not available.

We hypothesized that the strongly ionic character of EMIM-BF_4 plays a role in the activation of CO_2, which is otherwise fairly redox inactive. CO_2, however, is highly polarizable, as indicated by its quadrupole moment of −4.3 D Å (ref. [46]). The interaction of EMIM-BF_4 and CO_2 was simulated by DFT. A past study suggests that CO_2 can undergo complexation with the *N*-heterocyclic carbene, $EMIM^*$, formed from $EMIM^+$ by H^+ loss[42]. We investigated using DFT the structure of such a [EMIM*-CO_2] complex (Fig. 3a). The complex exhibits binding between the C atom of the CO_2 and the C_2 atom of the imidazole ring with an energy of intermolecular interaction, $E_{m\text{-}m}$, of −0.36 eV. This interaction is stronger than, for instance, the interaction of an H_2O molecule and CO_2 (Fig. 3b). Unlike the latter case, complexation with $EMIM^*$ leads to considerable restructuring of the CO_2 moiety. The CO_2 moiety adopts a bent configuration with an O=C=O angle of 133.7° and C=O bonds lengthened to 1.24 Å. In fact, the geometry of the CO_2 moiety in the complex closely mirrors that of the $CO_2^{\bullet-}$ anion radical, which has a bond angle of 137.8° and bond length of 1.23 Å (Supplementary Fig. 24). Moreover, from Mulliken charge partitioning analysis (Supplementary Fig. 25), the CO_2 moiety in the [EMIM*-CO_2] complex is found to have a net charge of −0.73, which indicates its partial anionic character.

It is known that the energetic cost of the drastic structural reorganization from linear CO_2 to the bent $CO_2^{\bullet-}$ anion radical poses a major barrier for e^- acceptance by CO_2 (refs. [37–42]). However, our DFT calculations show that in its complex with EMIM*, the CO_2 moiety is structurally pre-configured for e^- acceptance. Consistent with this finding, $1e^-$ addition to [EMIM*-CO_2] is much more favorable as compared with $1e^-$ addition to CO_2 (Fig. 3c, d). Thus, it appears that EMIM-BF_4 can promote the transfer of photogenerated e^- from the Au NP to adsorbed CO_2, which is otherwise a major kinetic bottleneck in the photocatalytic reduction process. Furthermore, it is plausible that the $CO_2^{\bullet-}$ anion radical formed on the Au surface by photo-initiated e^- transfer process has an enhanced lifetime due to solvation or complexation by $EMIM^+$ (Fig. 3e). A longer lifetime of this reactive intermediate would increase the probability of C–C coupling between the intermediates.

Empirical kinetic model. Although the DFT computations provide insight into the central role of EMIM-BF_4 in CO_2 activation, the volcano-type dependence of the CO_2RR activity on the IL concentration deserves an explanation. From the hydrolysis of EMIM-BF_4 known from past studies[47–50]:

$$\mathrm{EMIM-BF_4} + x\mathrm{H_2O} \rightarrow \mathrm{EMIM^+} + \left[\mathrm{BF_{4-x}(OH)_x}\right]^- + x\mathrm{HF} \quad (1)$$

where $x = 1$–4 and the complexation of CO_2 with $EMIM^+$ predicted in DFT simulations:

$$\mathrm{EMIM^+} + \mathrm{CO_2} \rightarrow [\mathrm{EMIM^*-CO_2}] + \mathrm{H^+} \quad (2)$$

we postulate a rate determining step in the reaction of CO_2

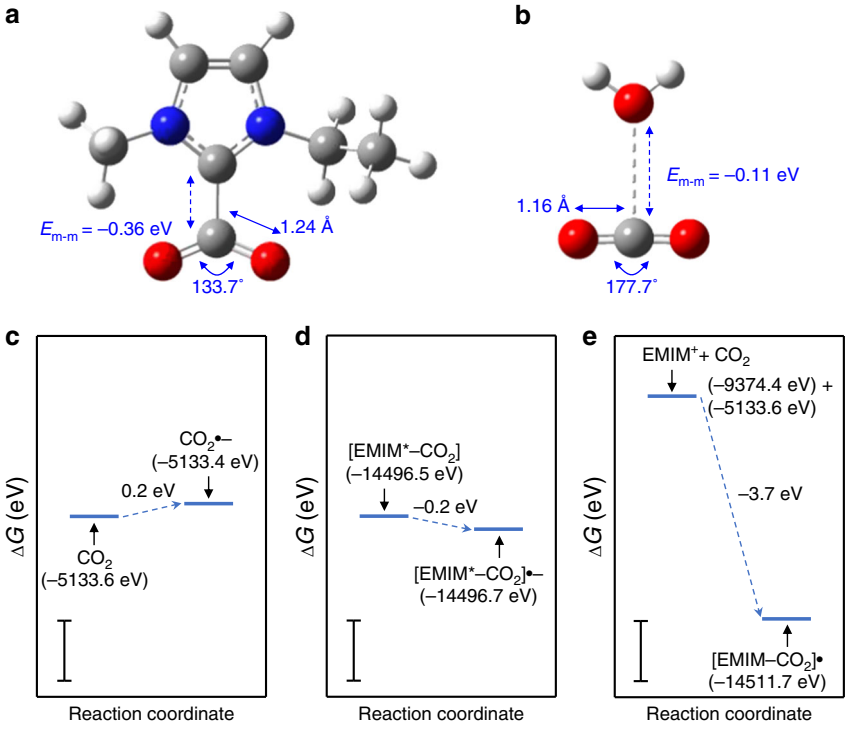

Fig. 3 The role of the ionic liquid in Au NP-photocatalyzed CO_2RR. **a**,**b** DFT-optimized geometries of [EMIM*-CO_2] (**a**) and [H_2O-CO_2] (**b**) complexes. C, H, O, and N atoms are depicted by gray, white, red, and blue spheres, respectively. Key bond lengths, bond angles, and the energy of intermolecular interaction, E_{m-m}, are indicated for each of the complexes. **c**–**e** DFT-computed free energy cost, ΔG, of formation of the 1e$^-$ adduct of CO_2 (**c**), 1e$^-$ adduct of [EMIM*-CO_2] (**d**), and 1e$^-$ adduct of CO_2 in the presence of EMIM$^+$ (**e**). In the latter case, the 1e$^-$ adduct of CO_2, $CO_2^{\bullet-}$, is stabilized by complexation with EMIM$^+$ as described by the net process: EMIM$^+$ + CO_2 + e$^-$→ [EMIM-CO_2]$^\bullet$. In **c**–**e**, the free energy of each species is indicated in parentheses. Scale bars are 1 eV in length

and H_2O:

$$\mathrm{EMIM-BF_4} + \mathrm{CO_2} + x\mathrm{H_2O} \rightarrow [\mathrm{EMIM^*-CO_2}] + \left[\mathrm{BF_{4-x}(OH)_x}\right]^- + (x+1)\mathrm{H^+} + x\mathrm{F^-} \quad (3)$$

From this reaction equation, the concentration of the activated CO_2 complex, [EMIM*-CO_2], is expected to be directly proportional to $[H^+]^{x+1}$. Therefore, the $[H^+]$ determined from the measured pH of the EMIM-BF_4 solution (Supplementary Fig. 23) serves as a proxy for the concentration of [EMIM*-CO_2], based on which the [EMIM*-CO_2] concentration is expected to be the highest in the EMIM-BF_4 concentration range around 5 mol%. The higher the concentration of the activated [EMIM*-CO_2] complex, the greater is the rate of CO_2 conversion and also the higher the likelihood of C–C coupling required for C_{2+} production. Therefore, both the overall activity and the selectivity in favor of C_{2+} products are favorable in the 3–7 mol% EMIM-BF_4 range, with the most optimal performance achieved at 5 mol% EMIM-BF_4. On the other hand, the activated complex has zero concentration in pure water on one extreme and in pure EMIM-BF_4 on the other extreme, which explains the nil turnover at these conditions. An additional reason for the drop in activity at higher EMIM-BF_4 concentrations may be that the adsorption of BF_4^- to the Au NP surface (Supplementary Fig. 26) dominates at these concentrations to such an extent that the adsorption of CO_2 and/or [EMIM*-CO_2] to the Au surface is largely inhibited and so is the e$^-$ transfer to CO_2.

The CO_2RR activity depends on the concentration of this activated complex to a high reaction order. This is best exemplified by the plots of TOF for each hydrocarbon as a function of the $[H^+]$ (Fig. 4a–e), which as explained above, serves as a proxy for the concentration of [EMIM*-CO_2]. The pseudo-reaction order, n, is found to be 1.9 for C_2H_4, 2.5 for C_2H_2, 3.7 for C_3H_6, and 4.0 for C_3H_8. The fit for the CH_4 TOF has a relatively high χ^2-value, so the n of 2.7 estimated for CH_4 has a lower confidence. In general, the pseudo-reaction order is higher for the longer hydrocarbons, which perhaps captures the need for multiple activated complexes to be available for undergoing coupling to C_2 and C_3 fragments. The high pseudo-reaction order for the C_3 products goes hand-in-hand with an apparent threshold in $[H^+]$ below which the TOF is zero or below the detection limit (Fig. 4d, e). For each of the hydrocarbon products, the $[H^+]$ raised to the power of the corresponding n follows a volcano trend with respect to the EMIM-BF_4 concentration, mirroring closely the trend in the TOF for that hydrocarbon (Fig. 4f–j).

Thus, we reported the green-light-driven synthesis of C_1–C_3 hydrocarbons from CO_2 and water on plasmonic Au NPs in an IL medium. The resonant green light absorption of the plasmonic NPs and their ability to sustain electrostatically charged surfaces under resonant CW excitation are at the heart of the observed photoreactivity. The IL plays a synergistic role due to its complexation with the CO_2, which preconfigures the CO_2 for accepting e$^-$ from photoexcited Au NPs. The enhanced reactivity of CO_2 in the presence of the IL obviates the need for an applied potential or a sacrificial scavenger. Although hydrocarbon production yields in the reaction need further optimization, the generation of propane by overall 20e$^-$–20H$^+$ reduction and coupling of three CO_2 molecules is both striking and mechanistically rich. The precise intermediates and reaction pathways, including C–C coupling and dehydrogenation steps, which yield each of the hydrocarbons, deserve further elucidation. Beyond CO_2 conversion studied here, ILs may have promise in other photocatalytic schemes where activation of relatively inert

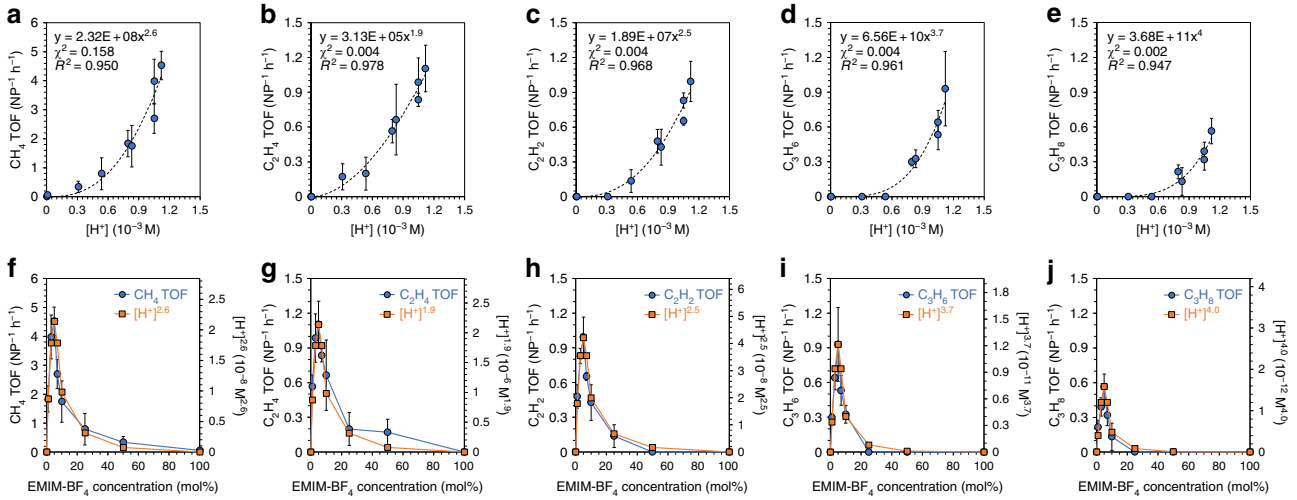

Fig. 4 Empirical kinetic model for the CO_2RR. **a**–**e** For each of the hydrocarbon products, the TOF is plotted as a function of the H^+ concentration, $[H^+]$, which serves as a proxy for the concentration of the [EMIM*-CO_2] complex. A fit to a power-law function $y = ax^n$ (dashed line) yields the fit parameter n, which represents the apparent reaction order in $[H^+]$. The best-fit equation is indicated for each plot along with the values of χ^2 and R^2, which serve as metrics of the goodness-of-fit. **f**–**j** For each hydrocarbon product, the TOF plotted as a function of the EMIM-BF_4 concentration follows a similar trend as the $[H^+]^n$, where n is the corresponding reaction order obtained from the plots in **a**–**e**. Each data point in **a**–**j** is the average of results from three identical trials and the error bar represents the SD of these measurements

substrates and stabilization of high-energy charged intermediates is desirable.

Data availability

All raw images and source data are available from the authors upon reasonable request.

Received: 15 November 2018 Accepted: 12 April 2019
Published online: 01 May 2019

References

1. Lewis, N. S. & Nocera, D. G. Powering the planet: chemical challenges in solar energy utilization. *Proc. Natl Acad. Sci. USA* **103**, 15729–15735 (2006).
2. Olah, G. A., Prakash, G. K. S. & Goeppert, A. Anthropogenic chemical carbon cycle for a sustainable future. *J. Am. Chem. Soc.* **133**, 12881–12898 (2011).
3. Chu, S. & Majumdar, A. Opportunities and challenges for a sustainable energy future. *Nature* **488**, 294–303 (2012).
4. Lewis, N. S. Research opportunities to advance solar energy utilization. *Science* **351**, 353 (2016).
5. Bai, S. et al. Highly active and selective hydrogenation of CO_2 to ethanol by ordered Pd–Cu Nanoparticles. *J. Am. Chem. Soc.* **139**, 6827–6830 (2017).
6. Xie, C. et al. Tandem catalysis for CO_2 hydrogenation to C2–C4 hydrocarbons. *Nano Lett.* **17**, 3798–3802 (2017).
7. Kattel, S., Ramírez, P. J., Chen, J. G., Rodriguez, J. A. & Liu, P. Active sites for CO_2 hydrogenation to methanol on Cu/ZnO catalysts. *Science* **355**, 1296–1299 (2017).
8. Vogt, C. et al. Unravelling structure sensitivity in CO_2 hydrogenation over nickel. *Nat. Catal.* **1**, 127–134 (2018).
9. Jiang, K. et al. Metal ion cycling of Cu foil for selective C–C coupling in electrochemical CO_2 reduction. *Nat. Catal.* **1**, 111–119 (2018).
10. He, J., Dettelbach, K. E., Salvatore, D. A., Li, T. & Berlinguette, C. P. High-throughput synthesis of mixed-metal electrocatalysts for CO_2 reduction. *Angew. Chem. Int. Ed.* **56**, 6068–6072 (2017).
11. Kuhl, K. P. et al. Electrocatalytic conversion of carbon dioxide to methane and methanol on transition metal surfaces. *J. Am. Chem. Soc.* **136**, 14107–14113 (2014).
12. Resasco, J. et al. Promoter effects of alkali metal cations on the electrochemical reduction of carbon dioxide. *J. Am. Chem. Soc.* **139**, 11277–11287 (2017).
13. Manthiram, K., Surendranath, Y. & Alivisatos, A. P. Dendritic assembly of gold nanoparticles during fuel-forming electrocatalysis. *J. Am. Chem. Soc.* **136**, 7237–7240 (2014).
14. Wuttig, A., Yoon, Y., Ryu, J. & Surendranath, Y. Bicarbonate is not a general acid in Au-catalyzed CO_2 electroreduction. *J. Am. Chem. Soc.* **139**, 17109–17113 (2017).
15. Wuttig, A., Yaguchi, M., Motobayashi, K., Osawa, M. & Surendranath, Y. Inhibited proton transfer enhances Au-catalyzed CO_2-to-fuels selectivity. *Proc. Natl Acad. Sci. USA* **113**, E4585–E4593 (2016).
16. Liu, M. et al. Enhanced electrocatalytic CO_2 reduction via field-induced reagent concentration. *Nature* **537**, 382–386 (2016).
17. Mariano, R. G., McKelvey, K., White, H. S. & Kanan, M. W. Selective increase in CO_2 electroreduction activity at grain-boundary surface terminations. *Science* **358**, 1187–1192 (2017).
18. Zeng, G. et al. Enhanced photocatalytic reduction of CO_2 to CO through TiO_2 passivation of InP in ionic liquids. *Chem. Eur. J.* **21**, 13502–13507 (2015).
19. Xing, M. et al. Modulation of the reduction potential of TiO_{2-x} by fluorination for efficient and selective CH_4 generation from CO_2 photoreduction. *Nano Lett.* **18**, 4–10 (2018).
20. Park, H., Ou, H. H., Colussi, A. J. & Hoffmann, M. R. Artificial photosynthesis of C_1-C_3 hydrocarbons from water and CO_2 on titanate nanotubes decorated with nanoparticle elemental copper and CdS quantum dots. *J. Phys. Chem. A* **119**, 4658–4666 (2015).
21. Rao, H., Schmidt, L. C., Bonin, J. & Robert, M. Visible-light-driven methane formation from CO_2 with a molecular iron catalyst. *Nature* **548**, 74–77 (2017).
22. Niu, K. et al. A spongy nickel-organic CO_2 reduction photocatalyst for nearly 100% selective CO production. *Sci. Adv.* **3**, e1700921 (2017).
23. Neaţu, Ş., Maciá-Agulló, J. A., Concepción, P. & Garcia, H. Gold–copper nanoalloys supported on TiO_2 as photocatalysts for CO_2 reduction by water. *J. Am. Chem. Soc.* **136**, 15969–15976 (2014).
24. Zhang, X. et al. Plasmon-enhanced catalysis: distinguishing thermal and nonthermal effects. *Nano Lett.* **18**, 1714–1723 (2018).
25. Zhang, X. et al. Product selectivity in plasmonic photocatalysis for carbon dioxide hydrogenation. *Nat. Commun.* **8**, 14542 (2017).
26. DuChene, J. S., Tagliabue, G., Welch, A. J., Cheng, W. H. & Atwater, H. A. Hot hole collection and photoelectrochemical CO_2 reduction with plasmonic Au/p-GaN photocathodes. *Nano Lett.* **18**, 2545–2550 (2018).
27. Hou, W., Pavaskar, P., Goeppert, A., Aykol, M. & Cronin, S. B. Photocatalytic conversion of CO_2 to hydrocarbon fuels via plasmon-enhanced absorption and metallic interband transitions. *ACS Catal.* **1**, 929–936 (2011).
28. Yu, S., Wilson, A. J., Heo, J. & Jain, P. K. Plasmonic control of multi-electron transfer and C-C coupling in visible-light-driven CO_2 reduction on Au nanoparticles. *Nano Lett.* **18**, 2189–2194 (2018).
29. Yu, S., Wilson, A. J., Kumari, G., Zhang, X. & Jain, P. K. Opportunities and challenges of solar-energy-driven carbon dioxide to fuel conversion with plasmonic catalysts. *ACS Energy Lett.* **2**, 2058–2070 (2017).
30. Yang, J., Guo, Y., Lu, W., Jiang, R. & Wang, J. Emerging applications of plasmons in driving CO_2 reduction and N_2 fixation. *Adv. Mater.* **30**, 1802227 (2018).
31. Calle-Vallejo, F. & Koper, M. T. M. Theoretical considerations on the electroreduction of CO to C_2 species on Cu(100) electrodes. *Angew. Chem. Int. Ed.* **52**, 7282–7285 (2013).

32. Nie, X., Esopi, M. R., Janik, M. J. & Asthagiri, A. Selectivity of CO_2 reduction on copper electrodes: the role of the kinetics of elementary steps. *Angew. Chem. Int. Ed.* **52**, 2459–2462 (2013).
33. Chen, Y., Li, C. W. & Kanan, M. W. Aqueous CO_2 reduction at very low overpotential on oxide-derived Au nanoparticles. *J. Am. Chem. Soc.* **134**, 19969–19972 (2012).
34. Kim, Y., Dumett Torres, D. & Jain, P. K. Activation energies of plasmonic catalysts. *Nano Lett.* **16**, 3399–3407 (2016).
35. Kim, Y., Wilson, A. J. & Jain, P. K. The nature of plasmonically assisted hot-electron transfer in a donor-bridge-acceptor complex. *ACS Catal.* **7**, 4360–4365 (2017).
36. Kim, Y., Smith, J. G. & Jain, P. K. Harvesting multiple electron-hole pairs generated through plasmonic excitation of Au nanoparticles. *Nat. Chem.* **10**, 763–769 (2018).
37. Rosen, Ba et al. Ionic liquid–mediated selective conversion of CO_2 to CO at low overpotentials. *Science* **334**, 643–644 (2011).
38. García Rey, N. & Dlott, D. D. Structural transition in an ionic liquid controls CO_2 electrochemical reduction. *J. Phys. Chem. C* **119**, 20892–20899 (2015).
39. Sun, L., Ramesha, G. K., Kamat, P. V. & Brennecke, J. F. Switching the reaction course of electrochemical CO_2 reduction with ionic liquids. *Langmuir* **30**, 6302–6308 (2014).
40. Asadi, M. et al. Nanostructured transition metal dichalcogenide electrocatalysts for CO_2 reduction in ionic liquid. *Science* **353**, 467–470 (2016).
41. Rosen, B. A. et al. In situ spectroscopic examination of a low overpotential pathway for carbon dioxide conversion to carbon monoxide. *J. Phys. Chem. C* **116**, 15307–15312 (2012).
42. Wang, Y. et al. Activation of CO_2 by ionic liquid EMIM–BF4 in the electrochemical system: a theoretical study. *Phys. Chem. Chem. Phys.* **17**, 23521–23531 (2015).
43. Fredlake, C. P., Crosthwaite, J. M., Hert, D. G., Aki, S. N. V. K. & Brennecke, J. F. Thermophysical properties of imidazolium-based ionic liquids. *J. Chem. Eng. Data* **49**, 954–964 (2004).
44. Zhang, Y., Shi, C., Brennecke, J. F. & Maginn, E. J. Refined method for predicting electrochemical windows of ionic liquids and experimental validation studies. *J. Phys. Chem. B* **118**, 6250–6255 (2014).
45. Zhou, M., Diwu, Z., Panchuk-Voloshina, N. & Haugland, R. P. A stable nonfluorescent derivative of resorufin for the fluorometric determination of trace hydrogen peroxide: applications in detecting the activity of phagocyte NADPH oxidase and other oxidases. *Anal. Biochem.* **253**, 162–168 (1997).
46. Pera-Titus, M. Porous inorganic membranes for CO_2 capture: present and prospects. *Chem. Rev.* **114**, 1413–1492 (2014).
47. Rosen, B. A., Zhu, W., Kaul, G., Salehi-Khojin, A. & Masel, R. I. Water enhancement of CO_2 conversion on silver in 1-ethyl-3-methylimidazolium tetrafluoroborate. *J. Electrochem. Soc.* **160**, H138–H141 (2012).
48. Freire, M. G., Neves, C. M. S. S., Marrucho, I. M., Coutinho, J. A. P. & Fernandes, A. M. Hydrolysis of tetrafluoroborate and hexafluorophosphate counter ions in imidazolium-based ionic liquids. *J. Phys. Chem. A* **114**, 3744–3749 (2010).
49. Kumar, B. et al. Renewable and metal-free carbon nanofibre catalysts for carbon dioxide reduction. *Nat. Commun.* **4**, 1–8 (2013).
50. Deetlefs, M., Pitner, W. R. & Hardacre, C. Quantification of halide in ionic liquids using ion chromatography. *Anal. Chem.* **76**, 2118–2123 (2004).

Acknowledgements

Funding for this work was provided by the Energy & Biosciences Institute (EBI) through the EBI-Shell program. GC-TCD calibration data were obtained from Andrew J. Wilson.

Author contributions

S.Y. performed all experimental studies, DFT computations, and data-analysis, and co-wrote the manuscript. P.K.J. conceived project and designed studies, analyzed results, and co-wrote the manuscript.

Additional information

Supplementary Information accompanies this paper at https://doi.org/10.1038/s41467-019-10084-5.

Competing interests: The authors declare no competing interests.

Reprints and permission information is available online at http://npg.nature.com/reprintsandpermissions/

Journal peer review information: *Nature Communications* thanks Jie Liu, Jianfang Wang, and the other, anonymous, reviewer(s) for their contribution to the peer review of this work

Publisher's note: Springer Nature remains neutral with regard to jurisdictional claims in published maps and institutional affiliations.